

Fault Slip Distribution of the 1999 M_w 7.1 Hector Mine, California, Earthquake, Estimated from Satellite Radar and GPS Measurements

by Sigurjón Jónsson,¹ Howard Zebker, Paul Segall, and Falk Amelung

Abstract We use a combination of satellite radar and GPS data to estimate the slip distribution of the 1999 M_w 7.1 Hector Mine Earthquake, a right-lateral strike-slip earthquake that occurred on a northwest-southeast striking fault in the southern California Mojave Desert. The data include synthetic aperture radar interferograms (InSAR) from both ascending and descending orbits, radar amplitude image offset fields (SARIO) for both ascending and descending azimuth directions, and campaign GPS observations from 55 stations provided by Agnew *et al.* (2002). We model the fault with nine segments derived from the field-mapped fault rupture, the SARIO data, and aftershock locations. We first estimate the dip of each fault segment, as well as a single constant strike-slip component across each segment, resulting in an average dip of 83° to the northeast and slip of up to 5.6 m. Then, we fix the optimal fault segment dip, discretize the fault segments into $1.5 \text{ km} \times 1.5 \text{ km}$ patches, and solve for the variable slip distribution using a nonnegative least-squares method that includes an appropriate degree of smoothing. Our preferred solution has both right-lateral strike slip and reverse faulting. The estimated geodetic moment is $5.93 \times 10^{19} \text{ Nm}$ (M_w 7.1), similar to seismological estimates, indicating that there are insignificant interseismic and postseismic deformation signals in the data. We find strike-slip displacements of up to 6.0 m and reverse faulting of up to 1.6 m, with the maximum slip located just northwest of the epicenter. Most of the slip is concentrated northwest and south of the epicenter; little slip is found on the northeastern branch of the fault. The SARIO data and our modeling indicate that the amount and extent of surface fault rupture were underestimated in the field.

Introduction

The M_w 7.1 Hector Mine earthquake occurred on 16 October 1999 in a remote and sparsely populated area of the Mojave Desert, southern California (Fig. 1). It was a right-lateral strike-slip event on a northwest-southeast oriented fault, with up to 5 meters of observed surface offset (Scientists of the USGS *et al.*, 2000). The Hector Mine earthquake involved rupture on the Buillon and Lavic Lake faults (Fig. 1), two previously mapped faults (Scientists of the USGS *et al.*, 2000). The Harvard Centroid Moment Tensor (CMT) solution for the earthquake has a moment of $5.98 \times 10^{19} \text{ Nm}$, rake of 174° , and fault dip of 80° to the northeast. A single-fault model derived from teleseismic data indicates that the rupture was bilateral, with a seismic moment of $6.0 \times 10^{19} \text{ Nm}$ (Ji, 2000). Inversion of strong motion data for slip distribution yields a dip of 77° , rake of 180° and a seismic moment of $6.7 \times 10^{19} \text{ Nm}$ (Kaverina *et al.*, 2002).

The Hector Mine earthquake occurred 7 years after the 1992 M_w 7.3 Landers earthquake, also a right-lateral strike-slip earthquake, on a parallel fault 20 km to the west. The Landers coseismic stress changes did not bring the Hector Mine hypocentral region closer to failure, as

the Coulomb stress change was negative (Scientists of the USGS *et al.*, 2000) unless the Hector Mine fault friction was high (Parsons and Dreger, 2000). However, viscoelastic modeling of postseismic ductile flow in the lower crust or upper mantle show gradual Coulomb stress increase during the 7 years between the two earthquakes (Freed and Lin, 2001; Zeng, 2001). These results suggest delayed triggering of the Hector Mine earthquake by viscoelastic stress transfer after the Landers event.

The Landers earthquake was the first earthquake that was imaged with synthetic aperture radar interferometry (InSAR) (Massonnet *et al.*, 1993; Zebker *et al.*, 1994). These studies demonstrated the usefulness of satellite radar data for observing crustal deformation and were the beginning of a number of spaceborne radar studies of crustal and ice deformation. Radar observations of the Landers area also shed new light on postseismic processes near fault zones, including vertical movements in fault step-overs due to pore-fluid flow (Peltzer *et al.*, 1996, 1998). Both InSAR and GPS measurements were used to estimate variations in slip along the fault in the Landers event (e.g., Hernandez *et al.*, 1999). The slip distribution was found to be heterogeneous with right-lateral strike slip of up to 7 m (Hernandez *et al.*, 1999).

¹Present address: Harvard University, Department of Earth and Planetary Sciences, 20 Oxford Street, Cambridge, Massachusetts

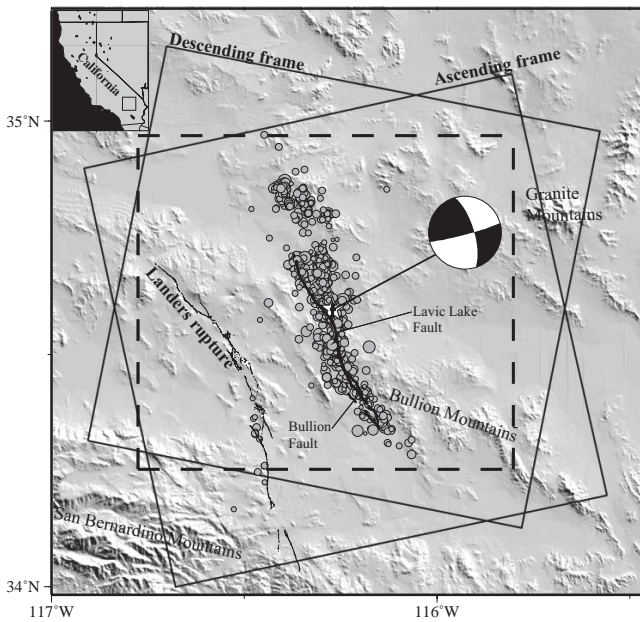


Figure 1. Shaded-relief topographic map of the area where the Hector Mine earthquake occurred in Mojave Desert, southern California (inset shows California). Mapped surface fault rupture is shown as thick line (Scientists of the USGS *et al.*, 2000), the epicenter is denoted with a star, and aftershocks during the first month following the earthquake are shown as circles (Hauksson *et al.*, 2002). The surface rupture of the 1992 Landers earthquake is shown as thin line. Rectangles show the area covered by the descending and ascending radar scenes. Dashed rectangle shows the area covered in Figs. 2-3 and 9-10.

In this study we use satellite InSAR data with multiple acquisition geometries from ascending and descending orbits along with radar image azimuth offset fields and GPS data to estimate spatial slip variations along the Hector Mine rupture. Among the questions we address are the following: Where was the slip concentrated on the Hector Mine rupture? How well can we resolve fault slip with these data? How was slip partitioned amongst segments of the complex rupture? Was there a significant dip-slip component in the earthquake, or was it a pure strike-slip event?

Data Analysis

Radar Interferograms

We used radar data acquired by the European radar satellites ERS-1 and ERS-2 before and after the earthquake from both ascending and descending orbits (Table 1). We formed interferograms by calculating the phase difference between two radar images. The interferometric phase difference contains information about deformation occurring between the two passes, as well as about the topography of the imaged area. We remove the topographic signature by forming additional short-term interferograms that contain topographic information only (no deformation) and subtracting this signal component from our original interferograms. The remaining phase difference is a measure of

the ground displacement in the line of sight (LOS) to the satellite. The ERS radar incidence angle is approximately 23° from vertical, so the measurements are most sensitive to vertical ground displacements. The measured interferometric phase is measured modulo 2π (wrapped) and needs to be integrated (unwrapped) to determine absolute LOS displacements. The interferograms were unwrapped using a statistical minimum cost-flow unwrapping algorithm optimized for deformation interferograms (Chen and Zebker, 2001). The coherence of the interferograms is generally high, because of the dry and stable surface condition in Mojave Desert, which results in reliable unwrapping.

Table 1
Interferograms Used in This Study.

Interferogram	Scene 1	Scene 2	T_{\perp}	B_{\perp}
Deformation (descending pass)	Orbit 23027 15 Sept. 1999	Orbit 23528 20 Oct. 1999	35 days	21 m
Deformation (ascending pass)	Orbit 2937 12 Nov. 1995	Orbit 23979 21 Nov. 1999	4 years	55 m
Topography (descending pass)	Orbit 24664 (E1) 3 Apr. 1996	Orbit 4991 4 Apr. 1996	1 day	114 m
Topography (ascending pass)	Orbit 23111 (E1) 16 Dec. 1995	Orbit 3438 17 Dec. 1995	1 day	310 m

All scenes were acquired by the ERS-2 satellite except those marked by E1 that are from ERS-1. T_{\perp} is the time separation between the two satellite passes and B_{\perp} is the perpendicular baseline.

Figure 2 shows the ascending and descending deformation interferograms. The two interferograms are dissimilar, due to different viewing geometries (arrows in Fig. 2). The descending interferogram (Fig. 2a) shows positive LOS displacement east of the fault, as the east side moved to the south (right-lateral strike slip), and negative LOS displacement west of the fault. In the ascending interferogram (Fig. 2b) the radar look direction is perpendicular to the fault strike, and fault parallel ground displacements cause no LOS displacements. In this case the interferogram shows four LOS displacement quadrants. The northwest quadrant exhibits strong positive LOS displacement, as horizontal displacements are towards the radar (away from the fault) and because it is a compressional quadrant (with uplift) of this right-lateral strike-slip fault. The southwest quadrant shows strong negative LOS displacement, as the ground moved away from the radar towards the fault and the area subsided. The LOS displacements of the northeast and southeast quadrants are smaller because of cancelling effects. In the northeast, positive LOS displacement from horizontal displacement towards the fault and negative LOS displacement from ground subsidence tend to cancel each other in this extensional quadrant. Similarly, in the southeast compressional quadrant we have uplift (positive LOS) and eastward horizontal displacement (negative LOS), resulting in almost no LOS displacement.

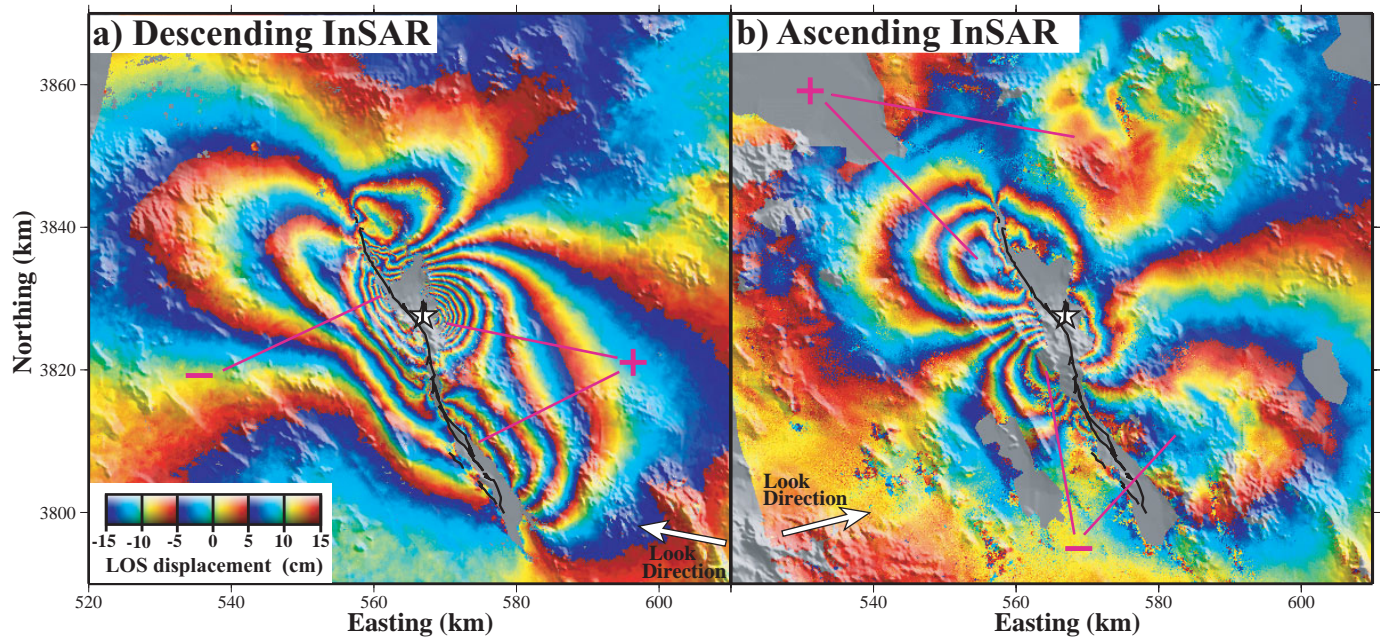


Figure 2: (a) Descending and (b) ascending interferograms showing the deformation of the Hector Mine earthquake. Each color cycle represents 10 cm of line-of-sight (LOS) displacement toward (yellow-red-blue) or away from (yellow-blue-red) the satellite. Arrows show the horizontal component of the look direction from the radar satellites. Purple + and – signs point to areas of positive and negative LOS displacement. The mapped fault trace is shown as thick line and the epicenter is denoted with a star. Coordinates are universal transverse Mercator (UTM) coordinates (zone 11S) in kilometers.

Azimuth Offsets of Radar Amplitude Images

When an interferogram is formed, the two radar scenes are coregistered to subpixel accuracy. Alignment follows from cross-correlation of local regions within the two radar amplitude (backscatter) images. Often it suffices to estimate the average offset between the two images at the top and the bottom of the two scenes and linearly interpolate in between; however, it is possible to estimate the offsets between the two amplitude images for many subimages to form a map of the offsets (Michel *et al.*, 1999a,b). We estimated the offset field using 32-pixel subimages and estimated the offsets for every 32 pixels in azimuth and 8 pixels in range. The ground-range resolution of radar images is 4 m in the azimuth direction (along track) and 20 m in the range direction (across track). The offsets were estimated to about 1/32 of a pixel or to about 12.5 cm in the azimuth direction. This offset field information can therefore be useful when horizontal displacements are large. We use here the term SARIO (synthetic aperture radar image offsets) data when referring to the azimuth offset fields.

The peak-to-peak amplitude of the SARIO data is ~ 6 m across the central part of the fault (Fig. 3), consistent with field estimates (Scientists of the USGS *et al.*, 2000). The descending SARIO image shows positive offset values on the east side of the fault as the east side moved to the south in the flight direction of the satellite (see arrow in Fig. 3a). In contrast, the ascending SARIO im-

age exhibits positive offsets on the west side of the fault, as the west side moved to the northwest in the ascending azimuth direction (Fig. 3b). The ascending SARIO data are noisier because the two ascending radar scenes span 4 years while the two descending scenes span only 1 month. Precise cross-correlation of small sub-images becomes increasingly difficult with longer time separation between radar images because erosion changes the ground surface over time.

Although the SARIO measurements are much noisier than the InSAR measurements, the azimuth SARIO data provide information about displacements that are perpendicular to the InSAR line-of-sight displacements (Fig. 3). The offsets also provide information near the fault trace, where no InSAR data are available due to decorrelation. Hence, the SARIO data can be used to determine the location of the fault trace if it is not previously well known (Peltzer *et al.*, 1999).

We do not use the range offset data because they are much noisier than the azimuth offsets, due to the low range resolution. The magnitude of the range offsets is also smaller than the magnitude of the azimuth offsets, because the surface displacements are mostly horizontal and parallel to the fault. Furthermore, the range offsets provide no significant additional information than provided by the InSAR data, as both are sensitive to displacements parallel to the radar look direction.

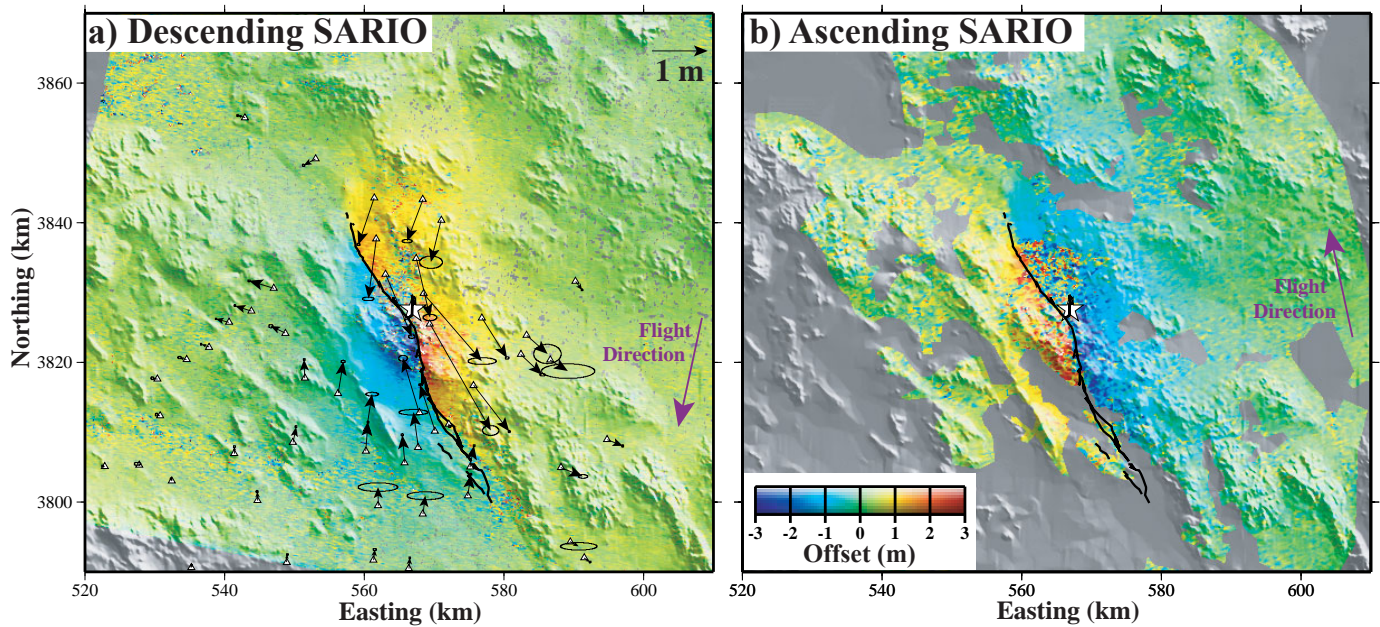


Figure 3: The synthetic aperture radar image offsets (SARIO) in the azimuth direction for (a) descending and (b) ascending orbits. Large purple arrows show the satellite flight direction in which the azimuth offsets are measured. The peak-to-peak amplitude of the offsets across the fault is about 6 m. Horizontal GPS campaign displacements (Agnew *et al.*, 2002) are overlaid on the offsets in (a). The mapped fault trace is shown as thick line and the epicenter is denoted with a star.

Campaign GPS Data

Campaign GPS data were provided by Agnew *et al.* (2002). Measurements were conducted at 55 stations 7–23 months before the earthquake and again after the earthquake (Fig. 3a). About half of the stations were observed in the first week following the earthquake, but some stations were observed as late as 6 months after the earthquake. The GPS displacements have been corrected for interseismic deformation but not for postseismic deformation (Agnew *et al.*, 2002). The estimated displacement uncertainties vary by more than an order of magnitude from one station to another (Table 2), but the average uncertainties for the east, north and vertical components are 3.3 cm, 1.5 cm, and 6.1 cm. The stations are nearly evenly distributed across the central and southern part of the fault, but few stations cover the area to the north (Fig. 3a). The largest observed horizontal displacement is 2.2 m at a station located 3 km east of the central part of the fault, just southeast of the epicenter (Fig. 3a).

Comparison between Datasets

The radar interferograms can be compared to the GPS data by projecting the GPS observations into the radar line of sight direction. The LOS unit vectors are given in Table 2. The root mean square (rms) differences between the GPS and the descending and ascending interferograms show 5.8 cm and 6.4 cm mismatch, respectively. The large differences may partly be explained by tilts in the images.

InSAR data exhibit large-scale tilts due to orbit uncertainties. When we corrected for our lack of precise orbit knowledge by removing the tilts, the rms differences between the GPS and the descending and ascending interferograms were reduced to 4.9 cm and 4.8 cm. The remaining large difference is caused by poor accuracy of the vertical component of the GPS displacements (Table 2), as the two sets of differences are found to be highly correlated. The radar LOS is 23° from vertical, so the vertical GPS component contributes 70% to the projected LOS value.

The SARIO data can also be compared to the GPS observations. In this case we project the horizontal GPS observations into the azimuth direction. The rms difference is found to be 15 and 40 cm for the descending and ascending SARIO images, respectively. The high rms value in the ascending case drops to 23 cm if two of the GPS stations are excluded. These two stations are located where the SARIO image is particularly noisy. The rms values above represent well the accuracy of the SARIO data, as the GPS horizontal displacements are much more precise than the azimuth offsets and can be treated as true displacements in this comparison.

Data Reduction

The multilooked radar interferograms used in this study are formed by averaging to $80 \text{ m} \times 80 \text{ m}$ pixels and consist of about 1.5 million points each. The deformation data are highly correlated spatially and can be reduced without losing significant information. We reduce the interferograms

Table 2
Information about the Datasets

Data Set	Data Size	Data Size Used	σ	Weight	Unit Vector
Descending InSAR	1.48×10^6	843	3 cm	49%	$[-0.38, 0.07, -0.92]$
Ascending InSAR	1.27×10^6	452	3 cm	26%	$[0.38, 0.08, -0.92]$
Descending SARIO	1.45×10^6	194	15 cm	2%	$[-0.19, -0.98, 0]$
Ascending SARIO	0.66×10^6	164	30 cm	1%	$[-0.21, 0.98, 0]$
GPS, east	55	55	0.6-19.4 cm	8%	$[1, 0, 0]$
GPS, north	55	55	0.6-7.0 cm	10%	$[0, 1, 0]$
GPS, vertical	55	55	0.7-30.7 cm	4%	$[0, 0, 1]$
Total	4.86×10^6	1818	-	100%	-

The size of the radar datasets is shown before and after quadtree partitioning. The estimated uncertainty is also shown, along with the weight that each dataset has. The unit vector shows the direction [East, North, Up] in which the datasets have sensitivity. The negative sign of the InSAR z-component is due to the fact that ground uplift is observed as range decreases.

InSAR, interferometric synthetic aperture radar; SARIO, synthetic aperture radar image offsets.

with a two-dimensional quantization algorithm known as quadtree [e.g., Welstead, 1999]. In this procedure, the scene is divided into four quadrants and the mean of each quadrant is calculated. If the rms scatter about the mean exceeds a given threshold, the quadrant is divided into four new quadrants, and the mean of each calculated and again compared with the data. The process continues iteratively until convergence. Data reduced in this manner then represent the statistically significant portion of the signal, with far fewer sampling points.

Figure 4 shows the quadtree result for the descending interferogram using an rms threshold of 2.83 cm (one-half radar wavelength). Although the rms noise of the interferogram far from the deformation is somewhat lower, we picked a higher threshold value to obtain a more manageable dataset size. The quadtree partitioning puts relatively few large squares away from the fault but many close to the fault where strong LOS gradients occur. The resulting 843 data points, 0.06% of the original ~ 1.5 million in the interferogram, can reconstruct the original interferogram within 2.83 cm uncertainty using bilinear interpolation. We also use this procedure for the ascending interferogram (same threshold) and for the SARIO images. The quadtree threshold is set to 15 and 30 cm for the descending and ascending SARIO data (Table 2).

After reduction of the InSAR and SARIO data, a total of 1818 datapoints remain (GPS included) making model computations more feasible. We treat all the observations as independent (diagonal covariance matrix) with estimated uncertainty of 3 cm for the InSAR data, 15 and 30 cm for the descending and ascending SARIO data, and scaled formal errors for the GPS data. From these uncertainties we can calculate the relative weight of the different datasets. The weight of the descending and the ascending InSAR data is 49% and 26%, 2% and 1% in case of the

descending and ascending SARIO data, and 22% in case of the GPS data.

Modeling

Inverse modeling is required to estimate spatial slip variations along the faults that ruptured in the Hector Mine earthquake from surface displacement measurements. We use analytical solutions that relate surface displacements to offsets across many small rectangular dislocations in a homogeneous elastic halfspace (Okada, 1992) to solve for slip using the geodetic data described above. The mapped surface offset of the Hector Mine rupture shows that the slip at surface varies from 0 to about 5 meters and that the fault is not a straight line (Fig. 1) (Scientists of the USGS *et al.*, 2000). Using only one rectangular dislocation with a constant slip is therefore an oversimplification, although it may lead to a reasonable first-order solution (Hurst *et al.*, 2000; see Table 3).

Fault Trace

Estimating the location, size, dip, orientation and slip across multiple rectangular dislocations is a numerically challenging task given the number of data points we have and the number of parameters we would need to estimate for these dislocations. We therefore use information from the mapped fault trace to constrain several parameters of the fault. We find that nine fault segments can reasonably represent the surface fault trace. For each of these segments we fix the location, length, and orientation such they agree with the mapped fault trace (Fig. 4b). At the two locations where the fault zone has major bends the fault appears to fork into two branches. At the southern bend we use the azimuth offset data to constrain the lo-

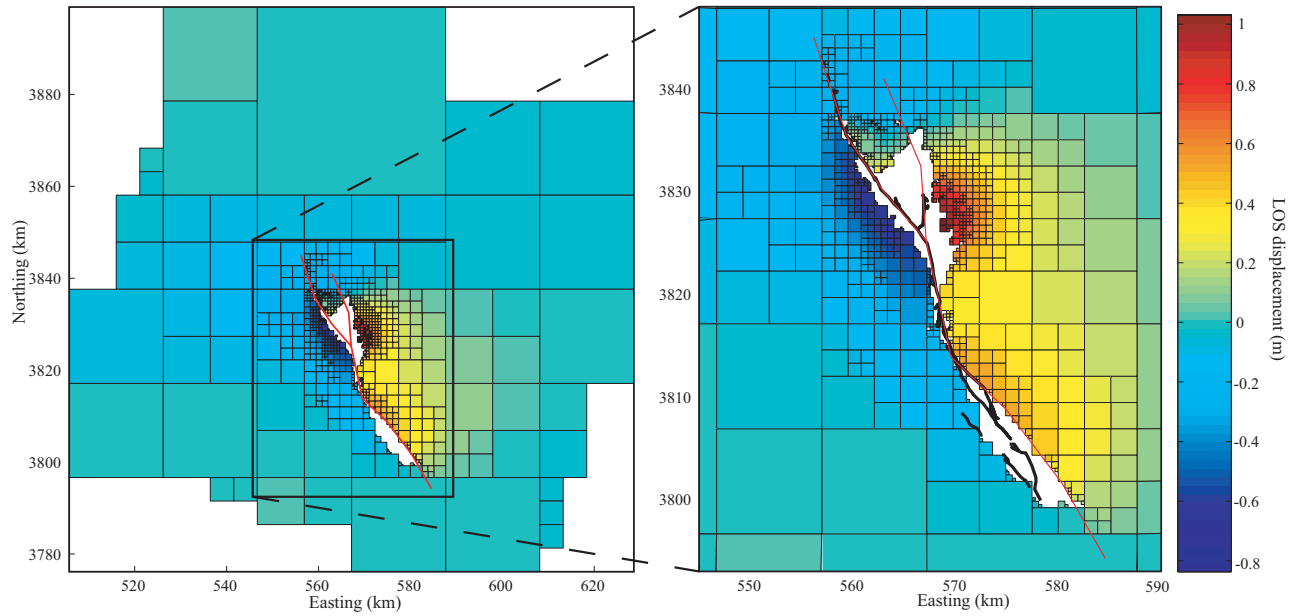


Figure 4: Quadtree partitioning of the descending interferogram, both the whole image (left) and a close up of the fault zone (right). This method reduced the number of data points from ~ 1.5 million to 843. The smallest rectangles are $360 \text{ m} \times 360 \text{ m}$. Also shown are the mapped fault trace (in heavy black lines) and the fault approximated as 9 segments (in red).

Table 3
Information about the Different Models

Model	N_d	n_p	ν	χ^2/ν	Dip	Max. s_1	Max. s_2	M_o (Nm)
Hurst - 1	1	6	1812	240	90°	3.8 m	0	3.72×10^{19}
Hurst - 2	1	8	1818	296	84.2°	3.0 m	1.5 m	3.79×10^{19}
Constant slip	9	18	1800	13.5	variable	5.6 m	0	7.08×10^{19}
Strike-slip only	714	714	-	-	83°	7.2 m	0	5.78×10^{19}
Preferred solution	714	1428	-	-	83°	6.0 m	1.6 m	5.93×10^{19}

N_d , number of dislocations used; n_p , number of parameters estimated; ν , degrees of freedom; χ^2/ν , normalized χ^2 sum; s_1 , estimated strike-slip component; s_2 estimated dip-slip component; M_o , estimated geodetic moment. Parameters of the first two models come from Hurst *et al.* (2000).

cation of our fault segments, as the mapped surface trace does not follow a regular pattern and does not extend as far southeast as the offset data indicate (Fig. 4b). At the northern bend, near the epicenter, we let the fault segments extend north of the mapped surface rupture as implied by aftershock activity (Hauksson *et al.*, 2002). We also fix the dip-slip displacement to 0 and the vertical extent of each fault segment to 15 km, the maximum depth of seismicity in the area (Deng *et al.*, 1998). These constraints decrease the number of parameters to be estimated for each of the nine fault segment from nine to two. The remaining parameters are the dip of each segment and the amount of strike-slip offset across the dislocations.

Fault Dip

The observed surface displacements \mathbf{d} can be described as a function g of the fault model parameters \mathbf{m} :

$$\mathbf{d} = g(\mathbf{m}) + \boldsymbol{\varepsilon}, \quad (1)$$

where $\boldsymbol{\varepsilon}$ are observational errors. Function g describes how slip across rectangular dislocation causes displacement at the ground surface [e.g., Okada, 1992]. The surface displacements are nonlinear functions of the fault dip; the slip components are linear. We seek the model \mathbf{m} that minimizes the L2-norm of the misfit function:

$$\Phi = \|\mathbf{W}(\mathbf{d} - g(\mathbf{m}))\|_2 \quad (2)$$

where \mathbf{W} is the weight matrix from Cholesky decomposition of the data covariance matrix inverse: $\mathbf{W}^T \mathbf{W} = \boldsymbol{\Sigma}^{-1}$. We find the optimal model using a simulated annealing

nonlinear searching scheme (Cervelli *et al.*, 2001) followed by a derivative-based method. The former method helps us to locate the valley that contains the global misfit minimum, and the second method brings us the bottom of that valley.

We solve for the dip and the strike-slip component of the nine fault segments. The resulting model has right-lateral strike-slip offset of up to 5.6 m and a geodetic moment of 7.08×10^{19} Nm (Table 3). The segment dips range from vertical to 72° to the northeast. The dips of the northern and central segments are better constrained than the dips of the southernmost segments. The average dip is 83° . This estimate agrees with a moment tensor solution derived from both broadband and strong motion data which has an 82° dip (Dreger and Kaverina, 2000), and it is similar to the result from finite-source modeling of strong motion data that yields 77° (Kaverina *et al.*, 2002). Our estimate is also similar to a single dislocation model solution of 84.2° estimated from GPS measurements (Hurst *et al.*, 2000).

Variable Strike Slip

To determine finer details of the strike-slip distribution we next discretize the fault segments into $1.5 \text{ km} \times 1.5 \text{ km}$ fault patches, extend the depth of each fault segment to 21 km down dip, and fix the dip of every fault segment to 83° . This restricted problem is linear and we can write equation (1) in matrix form as $\mathbf{d} = \mathbf{G}\mathbf{m}$, where \mathbf{d} is the data vector, \mathbf{m} is the vector of model parameters (strike-slip values for every patch), and \mathbf{G} are the data kernels relating the surface displacements to the model. The data require weighting as before and our weighted system of equation becomes:

$$\mathbf{d}' = \mathbf{G}'\mathbf{m}, \quad (3)$$

where $\mathbf{d}' = \mathbf{W}\mathbf{d}$ and $\mathbf{G}' = \mathbf{W}\mathbf{G}$.

To avoid oscillations in the fault slip we smooth the solution by additionally minimizing the two-dimensional second derivative (Laplacian) of the fault slip. We include the smoothing by solving for the following system of coupled equations:

$$\begin{bmatrix} \mathbf{d}' \\ \mathbf{0} \end{bmatrix} = \begin{bmatrix} \mathbf{G}' \\ \kappa^2 \mathbf{D} \end{bmatrix} \mathbf{m}, \quad (4)$$

where \mathbf{D} is a second-order finite difference operator (see Appendix) and the Lagrange multiplier κ^2 determines the weight of smoothing. We solve this system of equations using nonnegative least squares (Lawson and Hanson, 1974), i.e. only allowing for right-lateral strike slip.

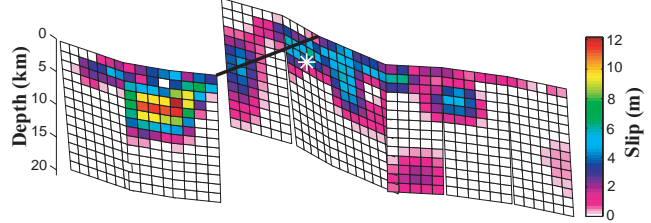
The smoothing parameter κ^2 depends on data weighting and on the number of data points; e.g., if we estimate two solutions, one by using all the data and one by only using the InSAR data, then two different values of κ^2 are needed to obtain equally smooth solutions. We therefore

define a new parameter, solution roughness, which is better suited to compare different solutions. The solution roughness is the average second-order finite-difference sum of each fault patch:

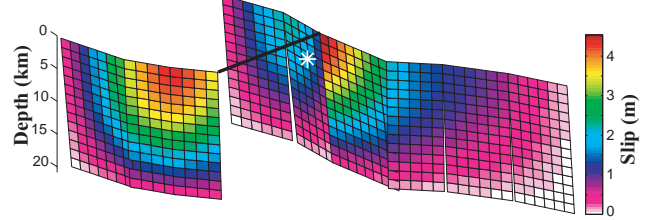
$$\rho = \frac{\sum_i |p_i|}{2N}, \quad (5)$$

where $\mathbf{p} = \mathbf{D}\mathbf{m}$ and N is the number of fault patches. The constant 2 is the result of smoothing the solution both along the fault strike and across strike. The units of ρ are cm/km, indicating the average slip gradient.

a) An under-smooth solution



b) An over-smooth solution



c) The final strike-slip solution

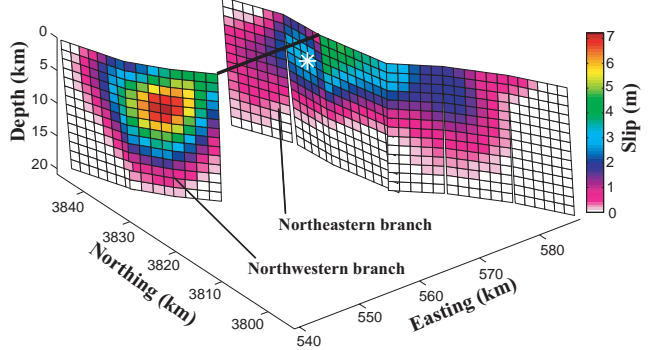


Figure 5. Estimated strike-slip distribution for three different smoothing weights. (a) Little weight on the smoothing resulting in an oscillatory solution ($\rho = 24$ cm/km). (b) Smoothing weight is strong resulting in a very smooth solution ($\rho = 0.9$ cm/km). (c) Final strike-slip solution, which has roughness of $\rho = 4.0$ cm/km. Star marks the Hector Mine hypocenter. The northwestern branch is shifted to the left for displaying purposes.

Figure 5 shows examples of strike-slip distribution solutions along the Hector Mine fault for three different smoothing weights. For a low smoothing weight ($\rho = 24$ cm/km) the fault slip is highly oscillatory with maximum slip of almost 12 m, and it is not likely to be plausible (Fig. 5a), but for a higher value of κ^2 ($\rho = 0.9$ cm/km) the slip distribution is overly smooth (Fig. 5b). The oscillatory and the overly smooth solutions result in moments

of 5.54×10^{19} Nm ($M_w 7.1$) and 6.48×10^{19} Nm ($M_w 7.2$), respectively. We choose the amount of smoothing from a trade-off curve with misfit function Φ (equation 2) plotted as a function of solution roughness ρ (Fig. 6). We pick a roughness of $\rho = 4.0$ cm/km for our final solution, as lower ρ results in significantly worse misfit but higher ρ does not improve the misfit much.

Our final strike-slip solution shows slip concentrated at the northwestern fault branch, with maximum slip of 7.2 m at 7 km depth (Fig. 5c). The estimated geodetic moment is 5.78×10^{19} Nm corresponding to a $M_w 7.1$ earthquake. The amount of slip sharply decays to zero north of the area of maximum slip, but it decays more slowly towards the south, where the area of high slip becomes shallower. The northeastern branch is found to have slip up to 3 m near the epicenter and 17% of the total moment; the northwestern branch has 50%. Very little slip is found below 15 km depth.

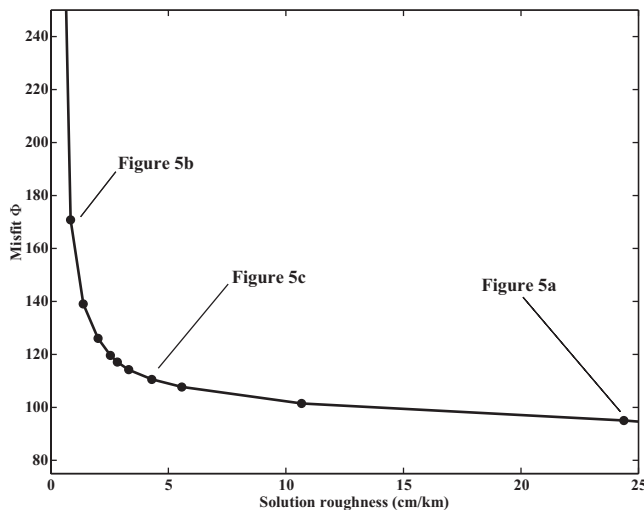


Figure 6. Trade-off curve with misfit function Φ plotted as function of average solution roughness ρ (equations 2 and 5). The misfit improves with increasing solution roughness. We pick a solution roughness of $\rho = 4.0$ cm/km. Additional slip roughness will not improve the misfit significantly.

Strike-Slip Distribution Determined from Each Dataset Independently

When the five datasets are used independently to determine the strike-slip distribution using the previously obtained solution roughness, similar solutions with strike slip concentrated on the northwestern branch result (Fig. 7). The differences between solutions describe each dataset's contributions to the optimal strike-slip solution. The solution based on the descending interferogram (weight 49%, Fig. 7a) is very similar to the final strike-slip solution (Fig. 5c). The main difference is that the descending InSAR solution shows up to 2 m of slip at the bottom of the

southern part of the fault, which is likely to be an artifact. The solution based on the ascending InSAR data (weight 26%, Fig. 7b) shows a slip maximum just south of the fault junction that extends into the northeastern branch. These data appear to be the main influence driving slip onto the northeastern branch in the final strike-slip solution near the epicenter (Fig. 5c).

The solution based on the descending SARIO data only (Fig. 7c) is quite similar to the final strike-slip solution, although these data have only 2% weight in the final solution. The ascending SARIO solution (weight 1%, Fig. 7d) has strong slip near the bottom of the fault that is likely to be an artifact. The GPS solution (weight 22%, Fig. 7e) appears to be similar to the optimal strike-slip solution (Fig. 5c), although it shows stronger slip on the shallow central part of the fault than the other solutions.

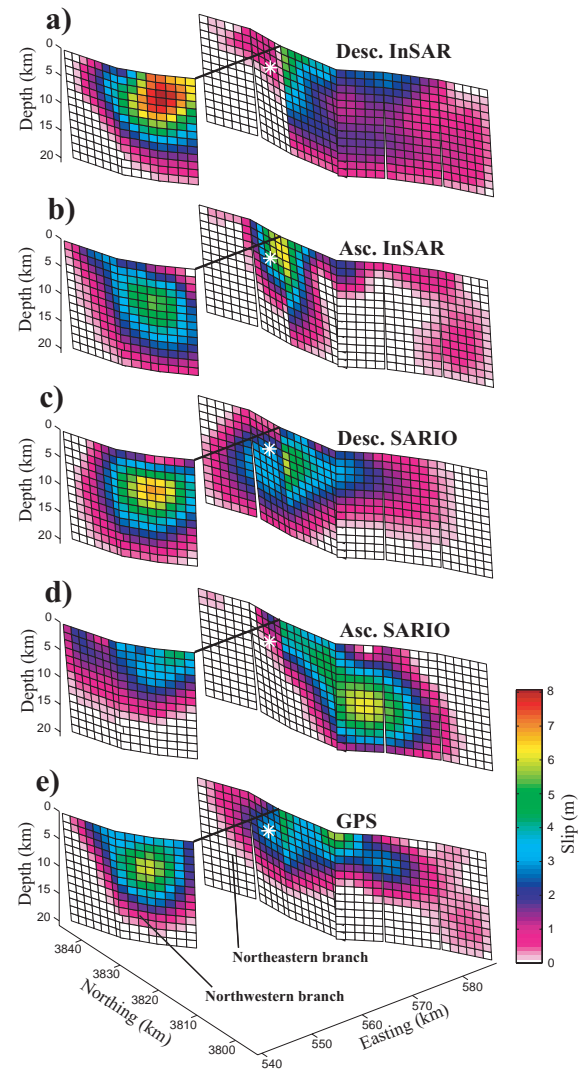


Figure 7. Strike-slip models using different datasets independently: (a) descending InSAR, (b) ascending InSAR, (c) descending SARIO, (d) ascending SARIO, and (e) GPS. All the solutions show strong right-lateral strike slip on the northwestern branch.

These results show that the GPS, descending InSAR, and even the descending SARIO data could have been used alone to derive the fault slip distribution fairly accurately. The fact that the ascending InSAR data result in a different slip distribution may indicate the importance of observing ground motion parallel to the main slip direction. The ascending InSAR radar look direction is perpendicular to the fault strike and not sensitive to fault parallel ground displacements.

Importance of Dip Slip

The Harvard Centroid Moment Tensor (CMT) solution for the Hector Mine earthquake has a rake of 174° and a fault dip of 80° to the northeast. Furthermore, another moment tensor solution from long period seismic data shows a rake of 175° and a fault dip of 70° to the northeast (Dreger and Kaverina, 2000). This may imply that the earthquake had a small amount of dip slip (reverse faulting) as well as right-lateral strike slip; however, inversion for slip distribution of strong motion data yields only a very low amount of dip slip (Kaverina *et al.*, 2002).

When we solve for both strike slip and dip slip on all the patches, the misfit decreases by 32%, 11%, and 8% in case of the InSAR, SARIO, and GPS data, respectively. The maximum strike slip is 6.0 m, and the maximum dip slip is 1.6 m (Fig. 8). In both cases the maximum slip is found on the northwestern branch, although the dip slip appears to be more localized than the strike slip. Interestingly, the strike slip of the northeastern branch decreases when dip slip is included, and this branch now has only 9% of the total moment, compared to 17% in the strike-slip-only solution. The seismic moment of the northwestern branch decreases as well, from 50% to 44%.

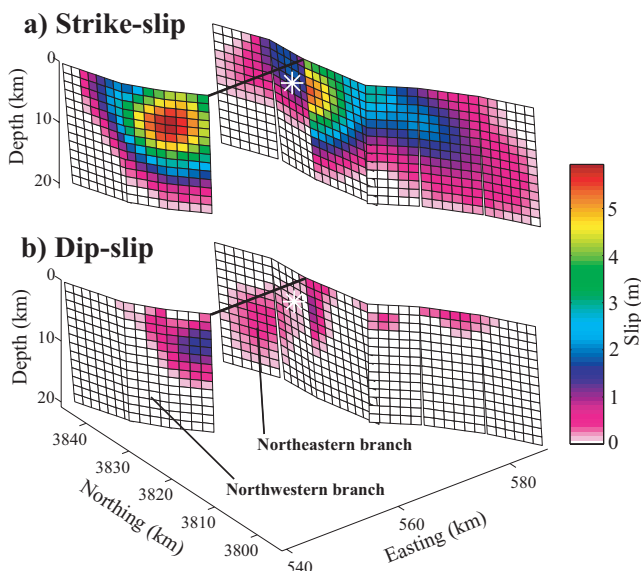


Figure 8. (a) Strike-slip and (b) dip-slip distribution of the preferred model. The model has up to 6.0 m of right-lateral strike slip and up to 1.6 m of reverse faulting.

But is the improvement in fit to the data significant? A common method to test a goodness of fit is the χ^2 test, calculating the normalized χ^2/v sum (where v is the degree of freedom; i.e., the number of data points minus the number of parameters estimated). Smoothing introduces correlations between the model parameters, so here we have no good way of calculating v . Therefore, we use cross-validation to find out if the fit improvement is significant. We take out the GPS observations and use all the InSAR and SARIO data to calculate two solutions, one with only strike slip and another one with both dip slip and strike slip. The fit to the GPS data improves by 15% when dip slip is included. This suggests that the amount dip slip that occurred is significant and our final preferred solution is the one that includes both strike slip and dip slip.

The total geodetic moment of our preferred solution is 5.93×10^{19} Nm ($M_w 7.1$), similar to the strike-slip-only solution (5.79×10^{19} Nm). The strike-slip component accounts for 92% of the moment and the dip-slip component 8%, resulting in an average rake of 175° , which agrees with the moment-tensor solutions. The fact we consistently obtain geodetic moments similar to seismologically derived estimates implies we have no significant amount of post-seismic or interseismic deformation in our geodetic data.

The InSAR data predictions of the final model resemble the data well (Figs. 2 and 9a-b). The residuals are largest close to the fault trace (Fig. 9c-d). The SARIO data predictions are qualitatively similar to the SARIO data, but large residuals occur near the fault (Figs. 3 and 10a-d). The GPS data predictions match the observations well, as shown in Figure 10e-f.

Comparison with Mapped Fault Offset

We also compare the mapped surface offset along the fault to the fault slip solutions and to the SARIO data. The mapped surface offsets show right lateral offset, varying from zero about 15 km north of the epicenter to a maximum of 5 m close to the epicenter (Fig. 11) (Scientists of the USGS *et al.*, 2000). The mapped surface slip decays to zero about 20 km south of the epicenter (Fig. 11).

We estimate the surface fault offset from the descending SARIO data (Fig. 3a) by comparing median filtered values on both sides of the fault every 0.5 km and projecting them into fault-parallel direction. The SARIO fault offset increases from 0 m in the north to 5 m just south of the epicenter (Fig. 11). The measurements show large scatter in the epicentral area, where the fault splits into two branches. The SARIO fault offset decays to zero about 40 km south of the epicenter.

The surface slip of the final preferred solution is similar to strike-slip-only solution with maximum slip of ~ 4.5 m in the epicenter area. Both fault-slip solutions are in agreement with the SARIO fault offset (the descending

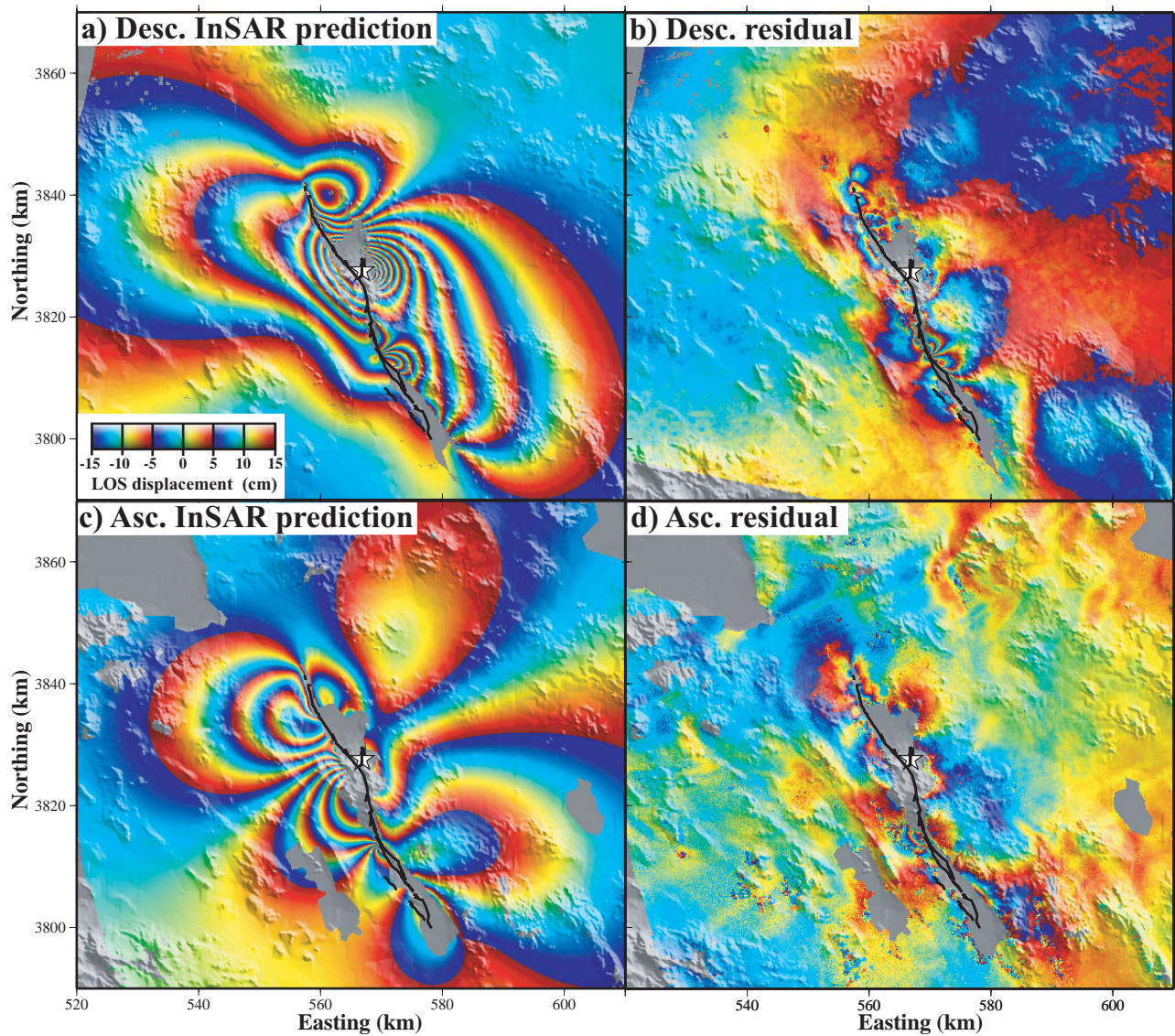


Figure 9: The model prediction and residuals for the InSAR observations. (a-b) Descending InSAR model prediction and the residual between the InSAR data (Fig. 2) and the model prediction. (c-d) Ascending InSAR model prediction and residual.

SARIO data have only 2% weight in the slip solutions). Both slip models and the SARIO data show more surface slip than mapped in the field, except in the epicentral area. In addition, our results indicate that the extent of the field mapped rupture was also underestimated. We find that surface slip extends 5 km further to the north and 15 km further to the south than detected in the field. This implies that field measurements of surface fault offset should be taken as a lower bound of the fault slip near surface.

Conclusions

We have estimated variations of the fault slip along the Hector Mine fault using a combination of five datasets:

descending and ascending interferograms, descending and ascending azimuth offset fields, and GPS observations. We find the surface fault trace to be sufficiently approximated by nine straight fault segments and we estimate that the average dip of these segments is 83° to the northeast. Our final preferred solution includes both right-lateral strike slip and reverse faulting. The maximum strike slip and dip slip are 6.0 m and 1.6 m at a depth of 6 km on the northwestern branch of the Hector Mine rupture, just northwest of the epicenter. The geodetic moment of the northeastern branch is only 9% of the total moment; the northwestern branch has 44%. The total geodetic moment is 5.93×10^{19} Nm ($M_w 7.1$), similar to seismological estimates. This indicates that no significant interseismic or postseismic deformation signal is seen in the geodetic

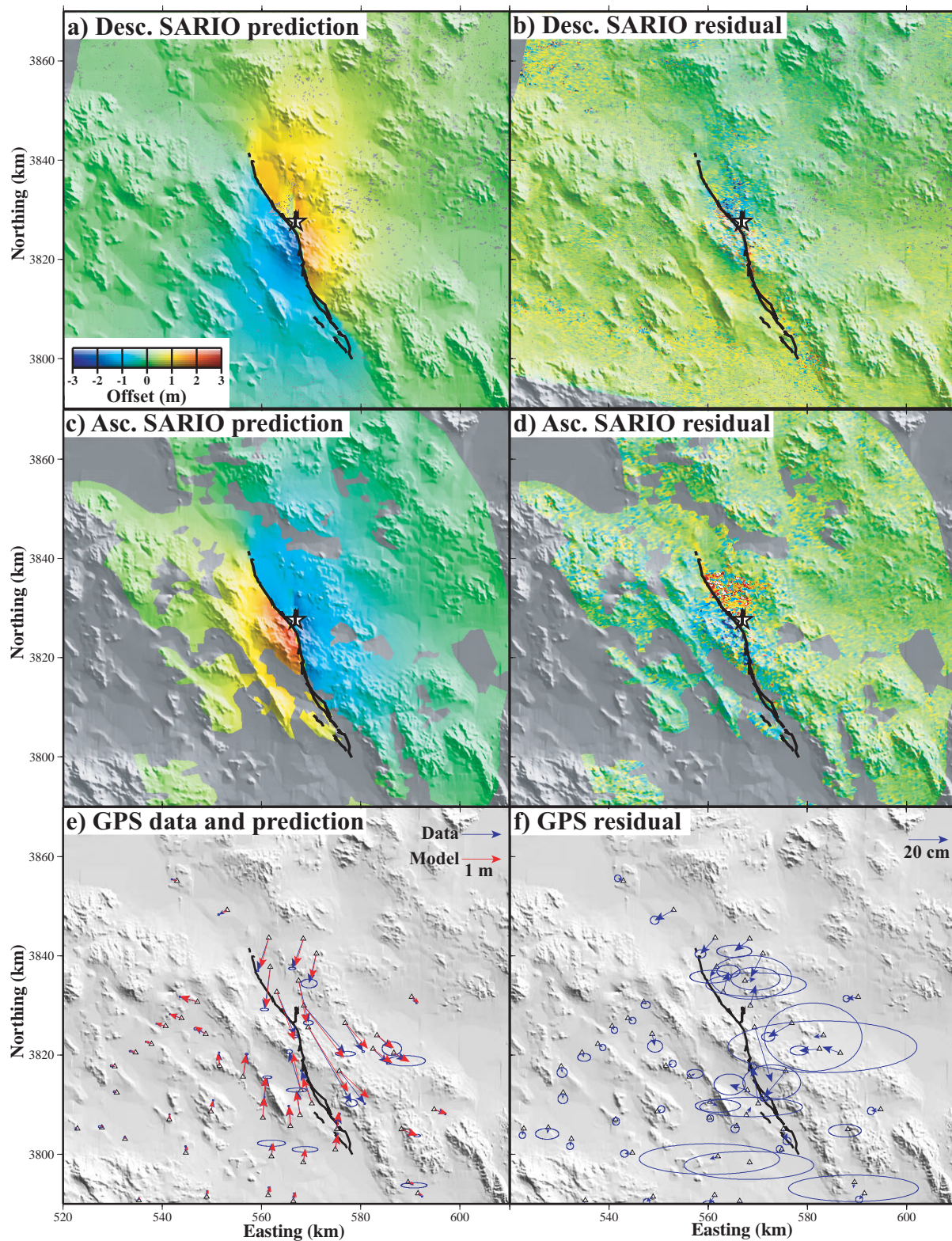


Figure 10: Model predictions and residuals for the SARIO and GPS data. (a-b) Descending SARIO model prediction and the residual between the SARIO data and the model prediction. (c-d) Ascending SARIO model prediction and residual. (e) Observed (blue arrows) and predicted (red arrows) horizontal GPS displacements. (f) Residual between the observed and predicted GPS displacements. Note different scales for arrows in (e) and (f).

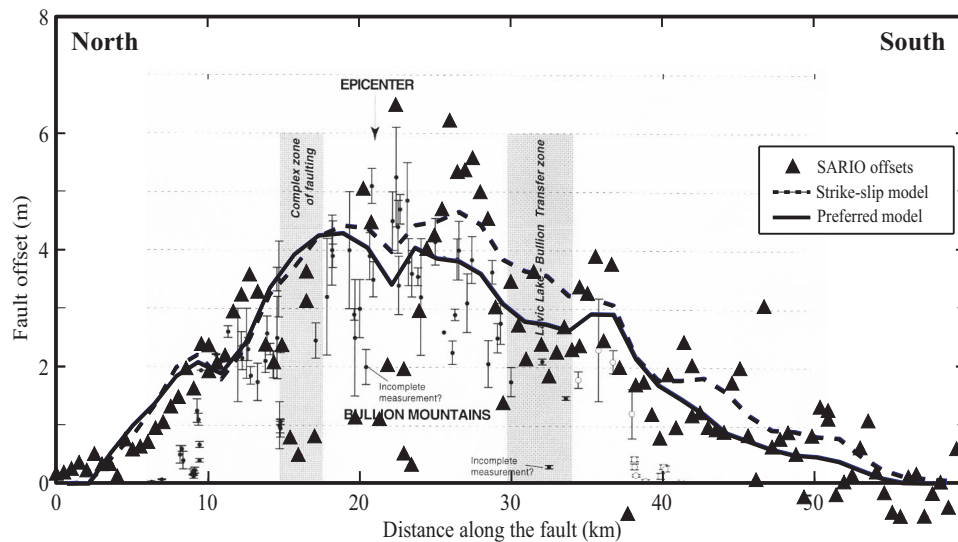


Figure 11: Comparison between surface fault offsets measured from the SARIO data (triangles), the surface slip of the final strike-slip model (dashed line), the preferred model (solid line), and the mapped fault offset (open and solid dots with error bars). The mapped fault offset was adopted from Scientists of the USGS *et al.*, (2000), where open dots represent cumulative slip estimates (slip values obtained by adding slip values from multiple parallel fault strands) and solid dots represent direct measurements. The SARIO data and the model results suggest that slip at surface continued 5 km further north and 15 km further south than detected in the field.

data. The SARIO data and the final model indicate that the amount and extent of the surface fault rupture were underestimated in the field.

Acknowledgments

Campaign GPS results were provided by Duncan Agnew (Scripps Institute of Oceanography). Curtis Chen (Stanford University) helped with the unwrapping and provided programs. Egill Hauksson (California Institute of Technology) provided aftershock locations. Thoughtful reviews by Pierre Briole and Barry Parsons greatly improved the paper. This work was supported by the National Science Foundation. Falk Amelung was supported by the SOEST Young Investigator program of the University of Hawaii (this is HIGP Contribution Number 1166 and SOEST Contribution Number 5825).

References

- Agnew, D. C., S. Owen, Z.-K. Shen, G. Anderson, J. Svarc, H. Johnson, K. E. Austin, and R. Reilinger (2002). Co-seismic displacements from the Hector Mine, California, earthquake: results from survey-mode GPS measurements, *Bull. Seism. Soc. Am.* **92**, 1355-1364 (this issue).
- Cervelli, P., M. H. Murray, P. Segall, Y. Aoki, and T. Kato (2001). Estimating source parameters from deformation data, with an application to the March 1997 earthquake swarm off the Izu Peninsula, Japan, *J. Geophys. Res.* **106**, 11,217-11,238.
- Chen, C. W., and H. A. Zebker (2001). Two-dimensional phase unwrapping with use of statistical models for cost functions in nonlinear optimization, *J. Opt. Soc. Am.* **18**, 338-351.
- Deng, J., M. Gurnis, H. Kanamori, and E. Hauksson (1998). Viscoelastic flow in the lower crust after the 1992 Landers, California, earthquake, *Science* **282**, 1689-1692.
- Dreger, D., and A. Kaverina (2000). Seismic remote sensing for the earthquake source process and near-source strong shaking: a case study of the October 16, 1999 Hector Mine Earthquake, *Geophys. Res. Lett.* **27**, 1941-1944.
- Freed, A. M., and J. Lin (2001). Delayed triggering of the 1999 Hector Mine earthquake by viscoelastic stress transfer, *Nature* **411**, 180-183.
- Hauksson, E., L. M. Jones, and K. Hutton (2002). The 1999 $M_w 7.1$ Hector Mine earthquake sequence: complex conjugate strike-slip faulting, *Bull. Seismol. Soc. Am.* **92**, 1154-1170 (this issue).
- Hernandez, B., F. Cotton, and M. Campillo (1999). Contribution of radar interferometry to a two-step inversion of the kinematic process of the 1992 Landers earthquake, *J. Geophys. Res.* **104**, 13,083-13,099.
- Hurst, K., D. Argus, A. Donnellan, M. Heflin, D. Jefferson, G. Lyzenga, J. Parker, M. Smith, F. Webb, and J. Zumberge (2000). The coseismic geodetic signature of the 1999 Hector Mine earthquake, *Geophys. Res. Lett.* **27**, 2733-2736.
- Ji, C. (2000). Slip history of 1999 Hector Mine, California earthquake (abstract), *Seism. Res. Lett.* **71**, 224.
- Kaverina, A., D. Dreger, and E. Price (2002). The combined inversion of seismic and geodetic data for the source process of the 16 October 1999 $M_w 7.1$ Hector Mine, California, earthquake, *Bull. Seismol. Soc. Am.* **92**, 1266-1280 (this issue).
- Lawson, C. L., and R. J. Hanson (1974). *Solving Least Squares Problems*, Prentice-Hall, Englewood Cliffs, New Jersey.
- Massonnet, D., M. Rossi, C. Carmona, F. Adragna, G. Peltzer, K. Feigl, and T. Rabaute (1993). The displacement field of the Landers earthquake mapped by radar interferometry, *Nature* **364**, 138-142.
- Michel, R., J.-P. Avouac, and J. Taboury (1999a). Measuring ground displacements from SAR amplitude images: application to the Landers earthquake, *Geophys. Res. Lett.* **26**, 875-878.

- Michel, R., J.-P. Avouac, and J. Taboury (1999b). Measuring near field coseismic displacements from SAR images: application to the Landers earthquake, *Geophys. Res. Lett.* **26**, 3017-3020.
- Okada, Y. (1992). Internal deformation due to shear and tensile faults in a half-space, *Bull. Seism. Soc. Am.* **82**, 1018-1040.
- Parsons, T., and D. S. Dreger (2000). Static-stress impact of the 1992 Landers earthquake sequence on nucleation and slip at the site of the 1999 $M = 7.1$ Hector Mine earthquake, southern California, *Geophys. Res. Lett.* **27**, 1949-1952.
- Peltzer, G., P. Rosen, F. Rogez, and K. Hudnut (1996). Post-seismic rebound in fault step-overs caused by pore fluid flow, *Science* **273**, 1202-1204.
- Peltzer, G., F. Crampé, and G. King (1999). Evidence of nonlinear elasticity of the crust from the $M_w 7.6$ Manyi (Tibet) earthquake, *Science* **286**, 272-276.
- Scientists of the U.S. Geological Survey, Southern California Earthquake Center, and California Division of Mines and Geology (2000). Preliminary report on the 10/16/1999 $M7.1$ Hector Mine, California earthquake, *Seism. Res. Lett.* **71**, 11-23.
- Welstead, S. T. (1999). *Fractal and wavelet image compression techniques*, SPIE Optical Engineering Press, Bellingham, Washington, 232 pp.
- Zebker, H. A., P. A. Rosen, R. M. Goldstein, A. Gabriel, and C. L. Werner (1994). On the derivation of coseismic displacement fields using differential radar interferometry: the Landers earthquake, *J. Geophys. Res.* **99**, 19,617-19,634.
- Zeng, Y. (2001). Viscoelastic stress-triggering of the 1999 Hector Mine earthquake by the 1992 Landers earthquake, *Geophys. Res. Lett.* **28**, 3007-3010.

Appendix: Smoothing Operator D

The slip solutions are smoothed by minimizing a second-order derivative (Laplacian) of the fault slip, in addition to the residual norm. As the slip is determined on discrete patches, we write the Laplacian as two-dimensional second-order finite-difference sum:

$$\frac{s_{i-1,j} - 2s_{i,j} + s_{i+1,j}}{(\Delta l_1)^2} + \frac{s_{i,j-1} - 2s_{i,j} + s_{i,j+1}}{(\Delta l_2)^2} \quad (A1)$$

where $s_{i,j}$ is the amount of slip on the patch in the i th row and j th column of the fault and Δl_1 and Δl_2 are the distances between adjacent patches (Fig. 12a).

Special care is needed where the fault forks into two branches. The slip of the elements just south of the junction are smoothed to the weighted sum of the slip on elements north of the junction (here we assume $\Delta l_1 = \Delta l_2 = 1$ km, to simplify the equations):

$$s_{i+1,j} + s_{i-1,j} + s_{i,j-1} + c_1 s_{i,j+1}^1 + c_2 s_{i,j+1}^2 - 4s_{i,j} \quad (A2)$$

where $s_{i,j+1}^1$ and $s_{i,j+1}^2$ are the slip values of the two branch patches north of the junction (Fig. 12b). The c_1 and c_2

are weight constants that depend on the orientation of the branches relative to the fault segment south of the junction:

$$c_1 = \frac{\cos \theta_1}{\cos \theta_1 + \cos \theta_2} \quad c_2 = \frac{\cos \theta_2}{\cos \theta_1 + \cos \theta_2} \quad (A3)$$

where θ_1 and θ_2 are strike deviations of the two branch segments from the strike of the south segment. Similarly, each of the segments north of the junction is smoothed to the slip south of the junction; e.g., a slip on a patch at the south edge of the northwestern branch would have the following finite difference sum:

$$s_{i+1,j+1}^1 + s_{i-1,j+1}^1 + s_{i,j+2}^1 + (1 - c_2)s_{i,j} - 4s_{i,j+1}^1 \quad (A4)$$

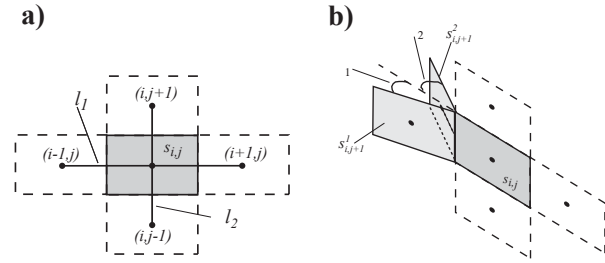


Figure 12. Schematic figure of fault patches. (a) A fault patch in the i th row and j th column is smoothed to patches at all sides. (b) The slip on a patch south of the junction is smoothed to a linear combination of the slip on the two branch patches north of the junction.

Department of Geophysics
Stanford University
Stanford, California 94305-2215
jonsson@pangea.stanford.edu
(S.J., P.S., H.Z.)

Hawaii Institute of Geophysics and Planetology
University of Hawaii
2025 Correa Road
Honolulu, Hawaii 96822
(F.A.)

Manuscript received 10 January 2001.